

XMM-NEWTON OBSERVATIONS OF EVOLUTION OF CLUSTER X-RAY SCALING RELATIONS AT  
 $Z = 0.4 - 0.7$ O. KOTOV<sup>1,2</sup> AND A. VIKHLININ<sup>2,1</sup>*The Astrophysical Journal, 2005 November*

## ABSTRACT

We present a spatially-resolved analysis of the temperature and gas density profiles of galaxy clusters at  $z = 0.4 - 0.7$  observed with *XMM-Newton*. These data are used to derive the total cluster mass within the radius  $r_{500}$  without assuming isothermality, and also to measure the average temperature and total X-ray luminosity excluding the cooling cores. We derive the high-redshift  $M - T$  and  $L - T$  relations and compare them with the local measurements. The high-redshift  $L - T$  relation has low scatter and evolves as  $L \propto (1+z)^{1.8 \pm 0.3}$  for a fixed  $T$ , in agreement with several previous *Chandra* and *XMM-Newton* studies (Vikhlinin et al., Lumb et al., and Maughan et al.). The observed evolution of the  $M - T$  relation follows  $M_{500} \propto E(z)^{-\alpha}$ , where we measure  $\alpha = 0.88 \pm 0.23$ . This is in agreement with predictions of the self-similar theory,  $\alpha = 1$ .

*Subject headings:* galaxies: clusters: general — surveys — X-rays: galaxies

## 1. INTRODUCTION

Scaling relations between the global cluster parameters such as total mass, X-ray luminosity, and average temperature are important tools for studies of galaxy clusters and their cosmological applications. Simple self-similar theory predicts that these relations have a power-law form,  $M \propto T^{3/2}$ , and  $L_{\text{bol}} \propto T^2$  (e.g., Kaiser 1991). Deviations of the observed relations from these theoretical expectations have been used to assess the role of non-gravitational processes in the cluster formation (see Voit 2005 for a recent review).

Of prime interest are relations between the total cluster mass and easily observed quantities, such as the average temperature of the intracluster medium (ICM) or X-ray luminosity. Such relations allow one to estimate mass functions for large samples of poorly observed clusters and use them for cosmological constraints. To derive the mass-observable relation requires accurate mass measurements in a representative sample of clusters. Establishing an accurate normalization of the  $M - T$  and  $M - L$  relations has been a focus of many recent observational and theoretical studies (Nevalainen et al. 2000; Evrard et al. 1996; Finoguenov et al. 2001; Reiprich & Boehringer 2002; Mathiesen & Evrard 2001; Sanderson & Ponman 2003; Borgani et al. 2004; Vikhlinin et al. 2005b; Kravtsov et al. in prep.).

X-ray observations of dynamically relaxed clusters can be used to infer the total mass via the hydrostatic equilibrium equation (e.g. Sarazin 1988). However, these are technically challenging observations that require accurate determinations of the cluster temperature profiles. X-ray mass measurements at radius  $r$  are only as accurate as  $T$  and  $dT/dr$  at that  $r$ . Simplifying assumptions, such as that the temperature is constant and gas density follows a  $\beta$ -model, lead to large biases in the mass determination (Markevitch & Vikhlinin 1997). Therefore, it is essential to have direct measurements of the ICM density and temperature distributions at large radii. Long-

exposure *Chandra* and *XMM-Newton* observations now provide such measurements for samples of low-redshift clusters (Vikhlinin et al. 2005a; Arnaud, Pointecouteau & Pratt 2005), and the resulting  $M - T$  relations are in very good agreement with the state-of-the-art cosmological simulations (Borgani et al. 2004; Kravtsov et al. in prep.).

In addition to normalization of the local scaling relations, cosmological applications require experimental constraints on their evolution at high redshifts. Several studies over the past few years have used *Chandra* and *XMM-Newton* observations of small samples of distant clusters to study evolution of the  $M - T$  relation (Ettori et al. 2004; Maughan et al. 2005). However, these works have used an isothermal  $\beta$ -model to infer cluster masses, which can bias results on evolution of the scaling relations.

In this *Paper*, we present a spatially-resolved analysis of *XMM-Newton* observations of a sample of 10 distant clusters spanning a range of temperatures and redshifts,  $2.5 < T < 9$  keV,  $0.4 < z < 0.7$ . The large effective area of *XMM-Newton* provides good statistical quality for most of the distant cluster data. The finite angular resolution of the *XMM-Newton* mirrors ( $\sim 4''$  FWHM or 24 kpc at  $z = 0.5$ ) is the main technical challenge in this analysis. However, this problem can be solved and deconvolved ICM temperature and density profiles can be restored for our distant clusters. We use these measurements to infer the total cluster mass, as well as the X-ray luminosity and temperature excluding the central cool regions, and thus study the evolution of cluster scaling relations at  $z > 0.4$ .

All distance-dependent quantities are derived assuming the  $\Omega_M = 0.3$ ,  $\Omega_\Lambda = 0.7$  cosmology with the Hubble constant  $H_0 = 71 \text{ km s}^{-1} \text{ Mpc}^{-1}$ . Statistical uncertainties are quoted at 68% CL.

## 2. OBSERVATIONS AND DATA REDUCTION

Our sample was selected from publicly available *XMM-Newton* observations of distant clusters. The final goal was to measure the cluster scaling relations at high redshift and we restricted our sample to objects with

<sup>1</sup> Space Research Institute, Moscow, Russia<sup>2</sup> Harvard-Smithsonian Center for Astrophysics, 60 Garden St., Cambridge, MA 02138

TABLE 1  
SUMMARY OF *XMM-Newton* OBSERVATIONS

Name	$t_{\text{PN}}^{\text{a}}$	$\delta_{\text{PN}}^{\text{b}}$	$t_{\text{MOS1}}^{\text{a}}$	$\delta_{\text{MOS1}}^{\text{b}}$	$t_{\text{MOS2}}^{\text{a}}$	$\delta_{\text{MOS2}}^{\text{b}}$
CL 0016+16.....	20.5	0.86	25.3	0.94	22.2	0.90
CL 0024+17.....	31.7	0.92	43.6	0.89	42.4	0.88
MS0302.5+1717.....	5.7	1.20	9.9	1.00	9.9	0.96
MS1054.4-0321.....	12.5	1.07	19.8	0.97	15.8	0.97
RXJ1120.1+4318.....	11.6	0.96	16.1	0.99	14.6	0.96
RXJ1334.3+5030.....	20.0	1.01	26.5	0.99	26.5	0.97
WJ1342.8+4028.....	17.8	1.07	27.6	1.02	25.3	1.01
WARPJ0152.7-1357.....	33.4	0.98	44.7	0.94	46.8	0.90
RXJ0505.3+2849.....	12.2	0.99	21.5	0.93	20.8	0.90
CL0939+472.....	20.7	0.91	30.5	0.85	30.5	0.82

<sup>a</sup> Clean exposure times, ksec.

<sup>b</sup> Ratio of observed 10–15 keV flux outside the field of view to that in the “closed dataset”.

$z \gtrsim 0.4$ . The selected clusters are listed in Table 1.

We used the data from all EPIC cameras (MOS1, MOS2, and PN). For data reduction, we used the *XMM-Newton* Science Analysis System (SAS) v6.0.0 and the calibration database with all updates available prior to November, 2004. All data were reprocessed with these latest versions of gain files. The initial data screening was applied using the recommended sets of event patterns, 0–12 and 0–4 for the MOS and PN cameras, respectively, and excluding all known bad CCD pixels. Our science goals required accurate background subtraction. The EPIC background is highly variable and only its quiescent component can be accurately modeled. Therefore, our next step was to detect and exclude the periods of flaring background. We extracted the light curves for each camera in the 2–15 keV band using the data from the entire field of view excluding detectable sources. The light curves were binned to 200 s time resolution and flares were detected as  $> 2\sigma$  deviations from the mean. Experiments with different choices of energy bands and flare detection thresholds have shown that our choice was close to optimal. For example, more flares are typically detected in the 2–15 keV band than in the frequently used  $> 10$  keV band because some flares are soft. In some observations, almost the entire exposure was affected by flares, and these observations had to be discarded. The clean exposure times for each camera are listed in Table 1.

To account for strong *XMM* mirror vignetting, we used an approach proposed by Arnaud et al. (2001). Each photon was assigned a weight proportional to inverse vignetting and these weights were then used in computing images and spectra. This was done using the SAS tool *evigweight*.

Background modeling in our analysis was implemented following the double-subtraction method of Arnaud et al. (2002). The first step of this method is to subtract the particle-induced background component. This component can be estimated from a set of *XMM* observations with the filter wheel closed (so called “closed data”). We compiled the closed dataset from public observations available in the *XMM* data archive; these data were reduced following steps identical to those of the science observations. The closed background was adjusted to the cluster observations using the observed flux in the 10–15 keV band outside the field of view. The scaling

factors are listed in Table 1. The second step is to determine the cosmic X-ray background (CXB) component. Its spatial distribution should be flat because vignetting correction is already applied. Therefore, the CXB spectrum can be measured in the source-free regions of the field of view, typically at  $r = 7' - 9'$  from the cluster center and then directly subtracted.

Finally, we computed corrections for photons registered during the CCD readouts (“out-of-time events”), using the SAS tools *epchain* and *emchain* with the *withouthoutoftime=yes* flag.

### 3. IMAGE ANALYSIS

We excluded all detectable point sources from the data in our spectral and spatial analysis. The sources were detected separately in the “optimal” 0.3–3 keV, “soft” 0.3–0.8 keV, and “hard” 2.0–6.0 keV energy bands. Detected point sources were masked with circles of 80% PSF power radii.

Spatial analysis of the cluster emission was performed in the 0.5 – 2.0 keV energy band. The images for each camera were corrected for vignetting and out-of-time events, with the particle background component subtracted as described in § 2, and analyzed independently. We extracted the azimuthally averaged surface brightness profiles centered on the X-ray surface brightness peak, even for clusters with irregular morphology (see below), excluding the CCD gaps and circles around the point sources. The obtained profiles were used to derive the parameters of the spatial distribution of the ICM, the cluster fluxes, and the background levels.

The cluster surface brightness profiles are often modeled with the so-called  $\beta$ -model,  $n_e^2 \propto (1 + r^2/r_c^2)^{-3\beta}$  or  $S_x \propto (1 + r^2/r_c^2)^{-3\beta+0.5}$  (Cavaliere & Fusco-Femiano 1976). However, this model poorly describes clusters with sharply peaked surface brightness profiles related to the radiative cooling of the ICM in the cluster centers. The simple modification of the  $\beta$ -model (Pratt & Arnaud 2002)

$$n_e^2 \propto \frac{(r/r_c)^{-\alpha}}{(1 + r^2/r_c^2)^{3\beta-\alpha/2}}, \quad (1)$$

allows adequately describing these cooling regions in the low redshift clusters. For  $\alpha = 0$ , this  $\alpha$ - $\beta$  model is identical to the usual  $\beta$ -model.

TABLE 2  
RESULTS OF IMAGE ANALYSIS

Name	$\beta$ fit				$\alpha - \beta$ fit			
	$z$	$\beta$	$r_c$ , kpc	$\chi^2/\text{dof}$	$\alpha$	$\beta$	$r_c$ , kpc	$\chi^2/\text{dof}$
CL 0016+16.....	0.54	0.76 $\pm$ 0.01	267.8 $\pm$ 7.8	176.4/128	0.64 $\pm$ 0.11	0.84 $\pm$ 0.03	372.7 $\pm$ 32.1	158.1/127
CL 0024+17.....	0.39	0.59 $\pm$ 0.02	89.0 $\pm$ 8.0	98.7/65	1.56 $\pm$ 0.13	0.72 $\pm$ 0.05	254.5 $\pm$ 58.8	78.3/64
MS0302.5+1717....	0.42	0.65 $\pm$ 0.06	118.7 $\pm$ 20.8	74.9/83	1.63 $\pm$ 0.23	1.03 $\pm$ 0.28	456.0 $\pm$ 963.7	69.0/82
MS1054.4-0321 <sup>a</sup> ...	0.82	...	...	...	...	...	...	...
RXJ1120.1+4318..	0.60	0.81 $\pm$ 0.04	203.8 $\pm$ 14.2	77.6/83	0.29 $\pm$ 0.40	0.84 $\pm$ 0.09	231.0 $\pm$ 60.1	77.4/82
RXJ1334.3+5030..	0.62	0.61 $\pm$ 0.02	127.7 $\pm$ 9.4	94.5/77	1.57 $\pm$ 0.27	0.95 $\pm$ 0.21	520.3 $\pm$ 665.9	87.2/76
WJ1342.8+4028....	0.70	0.49 $\pm$ 0.03	56.3 $\pm$ 15.5	40.7/56	2.03 $\pm$ 0.15	0.78 $\pm$ 0.21	579.1 $\pm$ 1690.5	35.1/55
WARPJ0152.7-1357 <sup>a</sup>	0.83	...	...	...	...	...	...	...
RXJ0505.3+2849..	0.51	0.69 $\pm$ 0.14	162.8 $\pm$ 46.2	103.1/96	1.07 $\pm$ 0.41	0.92 $\pm$ 0.26	353.2 $\pm$ 167.6	101.6/95
CL0939+472 <sup>a</sup> .....	0.41	...	...	...	...	...	...	...

<sup>a</sup>Profile fitting was not performed for irregular clusters

TABLE 3  
RESULTS OF SPECTRAL AND MASS DETERMINATION

Name	$T^a$	$Z^b$	$r_s^c$	$T_{500}^{spec\,d}$	$T_{500}^{em\,w\,e}$	$r_{500}$	$M_{500}$	$L_{bol}^f$
	(keV)	( $Z_\odot$ )	(Mpc)	(keV)	(keV)	(Mpc)	( $10^{14} M_\odot$ )	(erg s $^{-1}$ )
CL 0016+16.....	8.9 $\pm$ 0.3	0.17 $\pm$ 0.04	1.0	9.3 $\pm$ 0.4	9.4 $\pm$ 0.4	1.19 $\pm$ 0.05	8.83 $\pm$ 1.08	$50.79 \times 10^{44}$
CL 0024+17.....	3.5 $\pm$ 0.3	0.29 $\pm$ 0.06	0.5	3.6 $\pm$ 0.2	4.0 $\pm$ 0.3	0.74 $\pm$ 0.02	1.77 $\pm$ 0.16	$3.98 \times 10^{44}$
MS0302.5+1717....	4.5 $\pm$ 0.5	0.61 $\pm$ 0.27	0.5	4.1 $\pm$ 0.8	4.5 $\pm$ 0.9	0.78 $\pm$ 0.07	2.15 $\pm$ 0.63	$4.29 \times 10^{44}$
MS1054.4-0321....	7.5 $\pm$ 0.7	0.35 $\pm$ 0.09	0.7	...	...	...	...	$30.49 \times 10^{44}$
RXJ1120.1+4318.....	4.9 $\pm$ 0.3	0.41 $\pm$ 0.11	1.0	5.0 $\pm$ 0.3	5.1 $\pm$ 0.3	0.94 $\pm$ 0.07	4.64 $\pm$ 1.14	$13.04 \times 10^{44}$
RXJ1334.3+5030.....	4.6 $\pm$ 0.4	0.22 $\pm$ 0.14	0.8	4.6 $\pm$ 0.4	4.7 $\pm$ 0.4	0.78 $\pm$ 0.04	2.73 $\pm$ 0.48	$7.48 \times 10^{44}$
WJ1342.8+4028.....	3.5 $\pm$ 0.3	0.56 $\pm$ 0.29	0.6	3.1 $\pm$ 0.3	3.4 $\pm$ 0.4	0.59 $\pm$ 0.03	1.29 $\pm$ 0.24	$3.66 \times 10^{44}$
WARPJ0152.7-1357....	6.2 $\pm$ 0.4	0.33 $\pm$ 0.08	0.8	...	...	...	...	$21.71 \times 10^{44}$
RXJ0505.3+2849.....	2.5 $\pm$ 0.4	0.61 $\pm$ 0.42	1.0	2.8 $\pm$ 0.4	3.2 $\pm$ 0.5	0.65 $\pm$ 0.03	1.37 $\pm$ 0.23	$1.58 \times 10^{44}$
CL0939+472 .....	5.3 $\pm$ 0.2	0.22 $\pm$ 0.06	1.0	...	...	...	...	$10.05 \times 10^{44}$

<sup>a</sup> Best-fit temperature to the integral cluster spectrum.

<sup>b</sup> Best-fit metallicity to the integral cluster spectrum.

<sup>c</sup> Spectral extraction radius.

<sup>d</sup> Spectroscopic temperature within 70 kpc  $< r < r_{500}$ . Note that  $T_{500}^{sp\,c}$  was renormalized by +8% to account for *Chandra* vs. *XMM-Newton* cross-calibration.

<sup>e</sup> Emission-weighted temperature within 70 kpc  $< r < r_{500}$ .  $T_{500}^{ew\,e}$  was renormalized by +8% to account for *Chandra* vs. *XMM-Newton* cross-calibration.

<sup>f</sup> Bolometric luminosity within 70 kpc  $< r < 1400$  kpc. The central region was not excluded for clusters with irregular morphology, MS1054.4-0321, WARPJ0152.7-1357, CL0939+472. Emission-weighted temperature,  $T_{500}^{ew\,e}$ , was used to compute  $L_{bol}$  for all clusters except MS1054.4-0321, WARPJ0152.7-1357, CL0939+472.

The model for the observed surface brightness profiles can be obtained by numerical integration of eq.(1) along the line of sight and convolution of the result with the XMM PSF<sup>3</sup>. To represent the uniform sky X-ray background, we added a constant component to the model and treated it as a free parameter. The values of  $\alpha$ ,  $\beta$ , and  $r_c$  were derived from the joint fit to the observed profiles in the MOS1, MOS2, and PN cameras, with the overall normalizations and background levels fitted independently for each camera. For comparison, we also fitted the standard  $\beta$ -model by setting  $\alpha = 0$ . The obtained parameters for the  $\alpha$ - $\beta$  model and the standard  $\beta$  model fits are summarized in Table 2.

The best-fit ICM model was used to derive the total flux and the total mass from the hydrostatic equilibrium equation (see §6 below). Strictly speaking, eq.(1) can

<sup>3</sup> We used the latest available values of the King function parametrization of the MOS1, MOS2, PN PSF, see <http://xmm.vilspa.esa.es/docs/documents/CAL-TN-0018-2-4.pdf>

not be applied to the ICM distribution in clusters with irregular morphology. In these cases, the model fit was used only to measure the image background, and we do not list the values of  $\alpha$ ,  $\beta$ , and  $r_c$  in Table 2.

#### 4. SPECTRAL ANALYSIS

The cluster spectra were extracted in annuli and circles within radii listed in Table 3. The response matrices and effective area files were generated by the standard SAS tasks. Because the data were previously vignetting corrected, the effective area files were created for the on-axis position using the routine *arfgen*. The response matrices were generated in the spectrum extraction region via *rmfgen*. The spectra were binned, so that there were at least 20 counts per bin. The observed spectra were fitted in the 0.5 – 10 keV energy band. We checked that there were no prominent residuals near the instrumental lines and that exclusion of the instrumental line regions did not affect final results.

We used the Mewe-Kaastra-Liedahl plasma emission

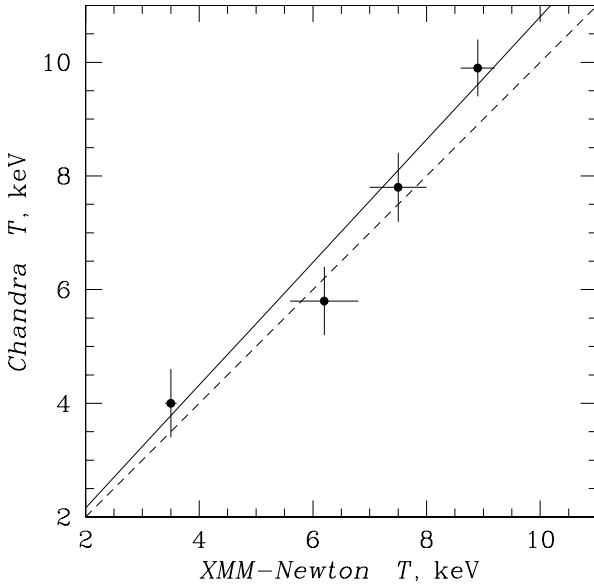


FIG. 1.— Comparison of *XMM-Newton* and *Chandra* temperatures. Dashed line corresponds to  $T_{XMM} = T_{Chandra}$ , and solid line shows the best-fit relation,  $T_{XMM} = 0.92 T_{Chandra}$ .

model (Mewe et al. 1985), with free metallicity and Galactic absorption fixed at the value derived from the radio surveys (Dickey & Lockman 1990). The EPIC-PN, MOS1, and MOS2 spectra for each extraction region were fitted jointly, with the spectral parameters tied and relative normalizations free. The resulting spectral parameters are listed in Table 3. Our single-temperature fits to wide-beam spectra are in good agreement with the published results (e.g., Lumb et al. (2004), Worrall & Birkinshaw (2003)).

## 5. THE CROSS-CALIBRATION BETWEEN XMM-NEWTON AND CHANDRA

To compare our results with the low-redshift scaling relations we need to correct for any systematic differences between *ASCA*, *Chandra*, and *XMM-Newton* measurements. Vikhlinin et al. (2002) verified that there is no systematic difference between the *Chandra* and the *ASCA* temperature measurements. Therefore we need to cross-calibrate only *XMM-Newton* and *Chandra*. Several of our clusters were in the Vikhlinin et al. (2002) sample. The comparison of *XMM-Newton* and *Chandra* temperatures for these clusters is shown in Fig. 1. There is a good overall agreement, although the *Chandra* temperature for the hottest cluster, CL0016+16, is marginally higher than our value. The linear fit gives  $T_{XMM} = (0.92 \pm 0.08) T_{Chandra}$ . A similar systematic difference is found in the comparison of the *Chandra* and *XMM* temperature profiles of nearby clusters (Vikhlinin et al. 2005a). We applied this correction factor to all temperature values because we use the *ASCA*  $L - T$  relation as low-redshift reference. For  $M - T$  relation, this correction is unimportant (see §7). Comparison of the cluster luminosities shows a good agreement, within  $\pm 5\%$ , between *Chandra* and *XMM*.

## 6. TEMPERATURE PROFILES AND MASS MODELING

The statistical quality of *XMM-Newton* data allows to reconstruct the temperature profiles from all our clusters. The main complication is that the XMM PSF size is non negligible compared with the angular size of distant clusters. For example, 50% of the flux from the central 100 kpc region ( $15''$  at  $z=0.6$ ) is scattered to larger radii ( $\approx 90\%$  of the flux stays within 260 kpc regions). The temperature in these regions is often lower than the cluster average because of radiative cooling, and hence this scattered flux can significantly bias the temperature measurements at large radii.

We corrected for the XMM PSF using an approach used for *XMM-Newton* data analysis by Pointecouteau et al. (2004). Using the best-fit  $\alpha$ - $\beta$  models of the cluster brightness and the XMM PSF calibration, we calculated the redistribution matrix,  $R_{ij}$ , of each temperature to each annulus that represents relative contribution of emission from annulus  $i$  to the observed flux in annulus  $j$ . The model spectrum,  $S_j$ , is then given by

$$S_j = \sum R_{ij} S(T_i), \quad (2)$$

where  $T_i$  is the temperature in annulus  $i$  and  $S(T_i)$  is the *mekal* spectrum for this temperature. Fitting this model to the observed spectra in all annuli simultaneously and treating all  $T_i$  as free parameters gives the deconvolved temperature profile. The raw and deconvolved temperature profiles are shown in Fig. 4–10.<sup>4</sup> The deconvolved temperature profiles are within  $1\sigma$  of the raw measurements in all cases. However the PSF correction is systematic and results in stronger temperature gradients. Thus neglecting this effect can slightly bias the mass measurements. In many cases, we observe a decrease of temperature at large radii, which is qualitatively consistent with the results for low-redshift clusters (Markevitch et al. 1998; De Grandi & Molendi 2002; Vikhlinin et al. 2005a). The only cluster that appears approximately isothermal is RXJ1120.1; our results for this cluster are fully consistent with the analysis by Arnaud et al. (2002). We fitted the observed temperature profiles by the function:

$$T(r) = T_0 \frac{1}{(1 + (r/r_0)^2)^\alpha} \quad (3)$$

A similar model describes the temperature profiles for low redshift clusters (Vikhlinin et al. 2005b). For local clusters,  $r_0$  scales with the average temperature as  $r_0 = 0.284 (T/1\text{ keV})^{0.537}$  Mpc (see Fig. 16 in Vikhlinin et al. (2005b)). The statistical uncertainties in our temperature profiles are insufficient to fit  $T_0$ ,  $r_0$ , and the outer slope  $\alpha$ . Therefore we fixed  $r_0$  at the value suggested by the low-redshift correlation, with an additional scaling,  $r_0 \propto 1/E(z)$ , to account for the redshift dependence of the virial radius for a fixed temperature (Bryan & Norman 1998).

To fit the observed profiles, we projected the 3-D model along the line of sight using the emission measure profile from the best fit  $\alpha$ - $\beta$  model. Projection was based on a weighting method that correctly predicts the best-fit

<sup>4</sup> The prime motivation for temperature profile analysis is to derive the total masses from the hydrostatic equilibrium equation. This cannot be done for irregular clusters, MS1054.4-0321, WARPJ0152.7-1357, CL0939+472, so we have not analyzed the temperature profiles in these cases.

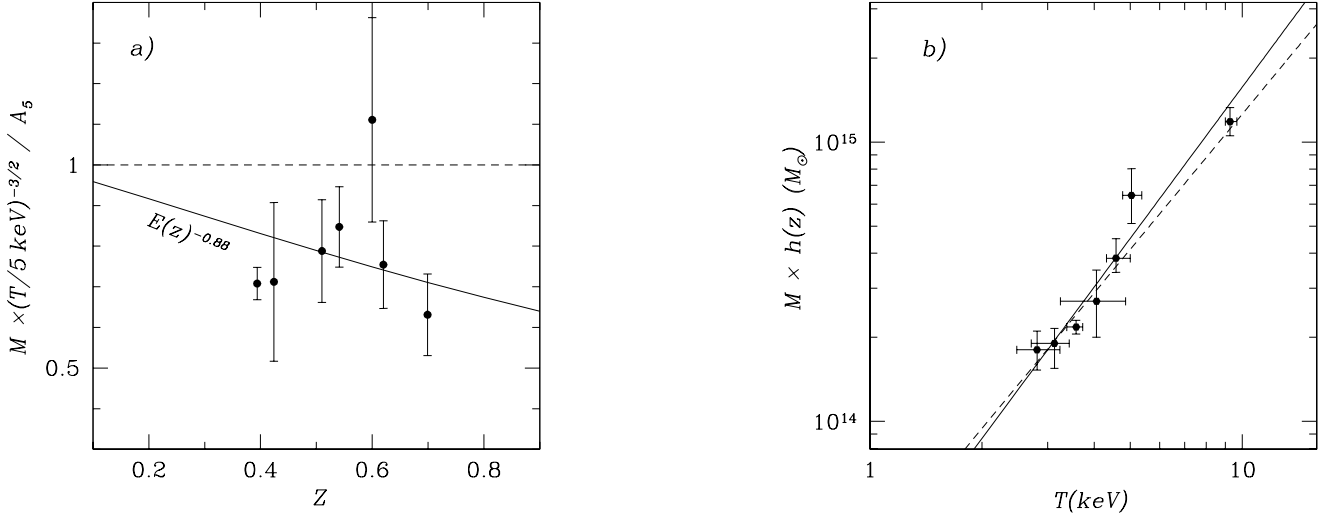


FIG. 2.— Correlation of cluster spectroscopic temperature and total mass. The data are corrected for the found *XMM-Chandra*(ASCA) systematic discrepancy in the temperature measurement. (a) The quantity  $a = M_{500}/T_{spec}^{1.5}/A_5$  as a function of  $z$ . The normalization  $A_5$  is adopted from *Chandra* observations of 13 low-redshift clusters (Vikhlinin et al. 2005b). (b) The solid line shows the derived best-fit  $M-T$  correlation. The dashed line shows the low-redshift result from Vikhlinin et al. (2005b).

spectral  $T$  for a mixture of different temperature components (Mazzotta et al. 2004; Vikhlinin 2005). For those clusters with the central temperature decrements we excluded the innermost bin from the fit. This procedure is correct because our temperature profiles were corrected for the XMM PSF. The obtained best-fit models are shown along with the deconvolved temperature profiles in Fig. 4–10.

Assuming hydrostatic equilibrium for the ICM, we can use the best fit temperature and density profiles to derive the total cluster masses:

$$M(r) = -\frac{rT(r)}{G\mu m_p} \left( \frac{d \log \rho(r)}{d \log r} + \frac{d \log T(r)}{d \log r} \right) \quad (4)$$

The mass was calculated within the radius that corresponds to the mean overdensity  $\Delta = 500$  relative to the critical density at the cluster redshift.

The uncertainties on the masses were calculated from Monte-Carlo simulations. The mass uncertainties are dominated by statistical uncertainties of the temperature profiles, and we neglected all other sources of error. We used the best-fit temperature profile as a template, applied Gaussian scatter with the  $rms$  equal to the statistical uncertainties, and fitted the simulated profile and derived the mass. The mass uncertainty was estimated as an  $rms$  scatter in 1000 simulations.

For each cluster we calculated the following temperature averages:

$T_{emw} - T(r)$  weighted with  $\rho_{gas}(r)^2$ .  $T_{emw}$  is needed to self-consistently compare the high- $z$   $L-T$  relation of our sample with the low-redshift result of Markevitch (1998).

$T_{spec} - T_{spec}$  is obtained by integrating a combination of  $T(r)$  and  $\rho_{gas}(r)^2$  as described in Vikhlinin (2005).  $T_{spec}$  is needed for comparison with the low-redshift  $M-T$  relation from Vikhlinin et al. (2005b).

$T_{spec}$  and  $T_{emw}$  were averaged in the radial range  $70 \text{ kpc} < r < r_{500}$ . The uncertainties on  $T_{emw}$  and  $T_{spec}$  were also calculated from Monte-Carlo simulations. The

obtained values of  $T_{emw}$ ,  $T_{spec}$ ,  $M_{500}$ , and the corresponding overdensity radius  $r_{500}$  are listed in Table 3. The  $r_{500}$  radii are also shown by vertical dotted lines in Fig. 4–10.

To test how background subtraction can affect our mass result, we checked two sources of uncertainties. First, we varied normalization of the article-induced component by  $\pm 10\%$ . Normalization of CXB component was varied by  $\pm 5\%$  (quoted XMM vignetting uncertainties). We refitted all spectra with renormalized background and repeated the mass analysis. The resulting variations in  $M_{500}$  were well within our statistical uncertainties.

## 7. EVOLUTION OF $M-T$ RELATION

Self-similar theory (e.g, Bryan & Norman (1998)) predicts that the relation between cluster mass and temperature is a power law that evolves as  $M_\Delta/T^{3/2} \propto E(z)^{-1}$ , where  $E(z) = H(z)/H_0 = (0.3(1+z)^3 + 0.7)^{1/2}$  for the adopted cosmology. Our measurements for distant clusters can be used to test these predictions.

The reference low-redshift  $M-T$  relation was adopted from a *Chandra* sample of Vikhlinin et al. (2005b), which is also close to the *XMM* results of Arnaud, Pointecouteau & Pratt (2005)). The *Chandra* sample contains 13 nearby clusters with exposures sufficient to measure temperature profiles to  $r \approx r_{500}$ . The temperatures of these clusters, 2–10 keV, match well the temperature range in our distant sample. Vikhlinin et al. (2005b) derived the mass-temperature relation,  $M_{500} = A_5(T_{spec}/5 \text{ keV})^{1.61 \pm 0.11}$ , where  $A_5 = (4.13 \pm 0.23)10^{14} M_\odot$ . The derived slope is consistent with the self-similar expectation,  $M \propto T^{3/2}$ .

Figure 2a shows the quantity  $a = M_{500}/T_{spec}^{1.5}/A_5$  as a function of  $z$  for our clusters. This quantity represents the normalization of the  $M-T$  relation as constrained by each cluster. For non-evolving  $M-T$  relation, all values of  $a$  would be consistent with 1. However, the observed values of  $a$  clearly indicate evolution. To quantify the

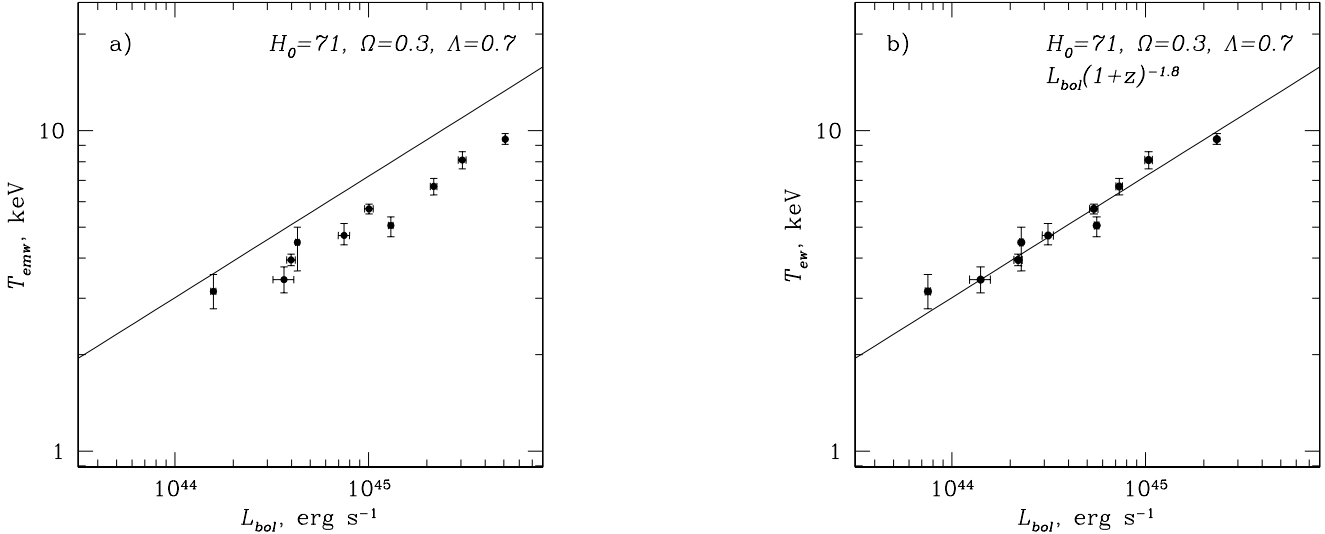


FIG. 3.— Correlation of cluster cooling flow corrected bolometric luminosity and  $T_{ew}$ . The data are corrected for the *XMM-Chandra*(*ASCA*) systematic discrepancies in the temperature and flux measurement. The solid line shows the  $L - T$  correlation for the low-redshift clusters (Markevitch 1998). (b) shows the correlation corrected by the obtained best-fit evolution factor,  $(1+z)^{-1.8}$ .

observed evolution, we fitted the data from Fig. 2a with a power law of  $E(z)$ ,  $a = E(z)^{-\alpha}$ . The best-fit index is  $\alpha = 0.88 \pm 0.23$ , where the error bar includes the uncertainties in low- $z$  normalization of the  $M - T$  relation and our high- $z$  mass measurements. The derived rate of evolution is consistent with the theoretically expected one,  $\alpha = 1$ . Therefore we can assume that the normalization of the  $M - T$  relation evolves exactly as  $A \propto E(z)^{-1}$ .

Now we can derive slope and normalization of the  $M - T$  relation defined by our distant clusters. For this, we corrected the mass measurements for evolution by multiplying them by  $E(z)$ . Figure 2b shows the corrected cluster masses as a function of temperature. The power-law fit,  $E(z)M = A_5(T/5\text{ keV})^\gamma$ , to distant clusters only<sup>5</sup> gives  $E(z)M_{500} = (3.21 \pm 0.31)(T_{spec}/5\text{ keV})^{1.79 \pm 0.19} \times 10^{14}h^{-1}M_\odot$ . The obtained value of the slope,  $\gamma = 1.79 \pm 0.19$  is statistically consistent with the value,  $\gamma = 1.5$ , predicted by the self-similar theory.

Finally, we note that the results on  $M - T$  relation are insensitive to the absolute calibration of the *XMM* effective area. The main effect of small calibration errors is to bias the derived temperatures by a constant factor. It follows from eq.(4) that the normalization of the  $M - T$  relation as given by individual clusters,  $A = M_\Delta / \langle T \rangle^{3/2}$ , is

$$A = \frac{(4/3\pi\Delta\rho_c)^{-1/2}}{(Gm_p\mu)^{3/2}} \left( \frac{T}{\langle T \rangle} \right)^{3/2} \left( -\frac{d\log\rho}{d\log r} - \frac{d\log T}{d\log r} \right)^{3/2}, \quad (5)$$

where the last two terms are evaluated at the overdensity radius,  $r_\Delta$ . Small calibration errors lead to small changes in estimated  $r_\Delta$  ( $\delta r_\Delta / r_\Delta \approx 0.5 \delta T / T$ ) but the normalization of  $M - T$  relation is not affected because both density and temperature are nearly power-law functions of  $r$  in the interesting range of radii.

<sup>5</sup> We used the bisector method modified to allow for both the measurement uncertainties and intrinsic scatter (Akitas & Bershady 1996).

## 8. THE X-RAY TEMPERATURE - LUMINOSITY CORRELATION

Our results can also be used to test the evolution in the cluster X-ray luminosity versus temperature relation. We performed at spatially-resolved analysis of the temperature and surface brightness profiles, including the PSF deconvolution. Therefore, we can directly exclude the contribution of the central cooling regions to both temperature and luminosity. This significantly reduces the scatter in the  $L - T$  relation (Markevitch 1998) and thus makes any evolution more prominent.

The X-ray bolometric luminosities were calculated using the Mewe-Kaastra-Liedahl plasma emission model. We used the measured best-fit temperatures for three objects with irregular X-ray morphology (MS1054.4-0321, WARPJ0152.7-1357, and CL0939+472) and the obtained emission-weighted temperatures for all other clusters. All temperatures were renormalized by +8% to account for *Chandra* versus *XMM-Newton* cross-calibration<sup>6</sup>. For the three objects with irregular X-ray morphology, we use the observed 0.5 – 2.0 keV counts rates within  $0 < r < 1.4$  Mpc as the normalizing fluxes. For all other clusters, the normalizing fluxes were calculated by subtracting from the observed 0.5 – 2.0 keV counts rates within  $0 < r < 1.4$  Mpc the fluxes calculated from the best-fit  $\alpha$ - $\beta$  models within  $r \leq 70$  kpc and multiplying the result by a factor of 1.06 to account for the flux within  $r \leq 70$  kpc in a typical  $\beta$ -model cluster (see (Markevitch 1998)). The resulting luminosities are listed in Table 3.

Figure 3 shows the resulting  $L - T$  relation. The solid line shows the relation for low-redshift clusters (Markevitch 1998). Clearly, distant clusters have higher luminosities for the given temperature. Parametrizing the

<sup>6</sup> Vikhlinin et al. (2002) demonstrated that there is no bias between *Chandra* and *ASCA* temperatures. Our *XMM* temperatures are on average 8% lower than the *Chandra* values, therefore we need to apply the temperature renormalization for a consistent comparison with the low- $z$  *ASCA* measurements by Markevitch (1998).

evolution as  $L = A(1+z)^\gamma T_{emw}^\alpha$ , we obtain  $\gamma = 1.8 \pm 0.3$  for  $\alpha$  fixed at the value for low-redshift sample,  $\alpha = 2.64$  (Fig. 3b). The observed rate of evolution is consistent with the results of Vikhlinin et al. (2002) obtained from an independent *Chandra* sample.

## 9. CONCLUSIONS

We presented a spatially-resolved analysis of the ICM density and temperature radial profiles in a sample of 10  $z > 0.4$  clusters observed with *XMM-Newton*. The main results can be summarized as follows.

We use the spatially-resolved measurements to study evolution of the  $L - T$  relation excluding the cluster cooling cores. The observed evolution of the bolometric luminosity for a fixed temperature is  $L \propto (1+z)^{1.8 \pm 0.3}$  in the redshift range  $z = 0.4 - 0.7$ , fully consistent with earlier *Chandra* results (Vikhlinin et al. 2002) and other *XMM-Newton* studies (Lumb et al. 2004; Maughan et al. 2005), but in apparent conflict with conclusions of Ettori et al. (2004).

Most of our clusters have non-constant temperature profiles. There is a temperature decline at large radii in most objects, which is qualitatively consistent with the temperature profiles in low-redshift clusters (Markevitch et al. 2004).

et al. 1998; De Grandi & Molendi 2002; Vikhlinin et al. 2005a).

Using the derived temperature and density profiles we determine the total cluster mass within the radius  $r_{500}$  without using the usual assumption of an isothermal  $\beta$ -model. This allows a direct comparison of the high-redshift  $M - T$  relation with the recent high-quality *Chandra* and *XMM-Newton* measurements for low-redshift clusters (Arnaud, Pointecouteau & Pratt (2005); Vikhlinin et al. (2005b)).

The observed  $M - T$  relation for distant clusters is  $E(z)M_{500} = (3.21 \pm 0.31)(T_{spec}/5\text{ keV})^{1.79 \pm 0.19} \times 10^{14} h^{-1} M_\odot$ . The derived slope,  $\gamma = 1.79 \pm 0.19$ , is statistically consistent with both  $\gamma = 1.61 \pm 0.11$  measured by Vikhlinin et al. (2005b) for low- $z$  clusters and  $\gamma = 1.5$  predicted by the self-similar theory.

We would like to thank M. Markevitch and B. Maughan for useful discussions. This work was supported by NASA grant NAG5-9217 and contract NAS8-39073. O. K. thanks SAO for hospitality during the course of this research.

## REFERENCES

- Akritas, M.G., & Bershady, M.A., 1996, ApJ, 470, 706  
 Arnaud, M., Neumann, D.M., Aghanim, N., et al., 2001, A&A, 365, L80  
 Arnaud, M., Majerowicz, S., Lumb, D., et al., 2002, A&A, 390, 27A  
 Arnaud, M., Pointecouteau, E., Pratt, G. W. 2005, A&A in press, (astro-ph/0502210)  
 Borgani, S., et al. 2004, MNRAS, 348, 1078  
 Bryan, G. L., & Norman, M. L. 1998, ApJ, 495, 80  
 Cavaliere, A., Fusco-Femiano, R., 1976, A&A, 49, 137  
 De Grandi, S., & Molendi, S. 2002, ApJ, 567, 163  
 Dickey, J. M. & Lockman, F. J. 1990, ARA&A, 28, 215  
 Ettori, S., Tozzi, P., Borgani, S., & Rosati, P. 2004, A&A, 417, 13  
 Evrard, A. E., Metzler, C. A., & Navarro, J. F. 1996, ApJ, 469, 494  
 Finoguenov, A., Reiprich, T. H., Böhringer, H. 2001, A&A, 368, 749  
 Kaiser, N. 1991, ApJ, 383, 104  
 Kirsch M., 07/28/2004, XMM-SOC-CAL-TN-0018  
 Lumb, D. H., et al. 2004, A&A, 420, 853  
 Markevitch, M., & Vikhlinin, A. 1997, ApJ, 491, 467  
 Markevitch, M., 1998, ApJ, 504, 27  
 Markevitch, M., Forman, W. R., Sarazin, C. L., & Vikhlinin, A. 1998, ApJ, 503, 77  
 Mathiesen, B. F., & Evrard, A. E. 2001, ApJ, 546, 100  
 Maughan, B. J., Jones, L. R., Ebeling, H., & Scharf, C. 2005, ApJ, submitted.  
 Mazzotta, P., Rasia, E., Moscardini, L., & Tormen, G. 2004, MNRAS, 354, 10  
 Mewe, R., Gronenschild, E. H. B. M., & van den Oord, G. H. J. 1985, A&AS, 62, 197  
 Nevalainen, J., Markevitch, M., & Forman, W. 2000, ApJ, 532, 694  
 Pointecouteau, E., Arnaud, M., Kaastra, J., & de Plaa, J. 2004, A&A, 423, 33  
 Pratt, G. W., Arnaud, M., 2002, A&A, 394, 375  
 Reiprich, T. H., Böhringer, H. 2002, ApJ, 567, 716  
 Sanderson, A. J. R., & Ponman, T. J. 2003, MNRAS, 345, 1241  
 Sarazin, C. L. 1988, X-ray Emission from Clusters of Galaxies (Cambridge: Cambridge University Press)  
 Vikhlinin, A., VanSpeybroeck, L., Markevitch, M. et al., 2002, ApJ 578, L107  
 Vikhlinin, A., 2005, ApJ, submitted, (astro-ph/0504098)  
 Vikhlinin, A., Markevitch, M., Murray, S. S., Jones, C., Forman, W., & Van Speybroeck, L. 2005a, ApJ, 628, 655  
 Vikhlinin, A., Kravtsov A., Forman, W., Jones, C., Markevitch, M., Murray, S. S., & Van Speybroeck 2005b, ApJ submitted, (astro-ph/0507092)  
 Voit, M. 2005, Rev. Mod. Phys., in press (astro-ph/0410173)  
 Worrall, D. M., & Birkinshaw, M. 2003, MNRAS, 340, 1261

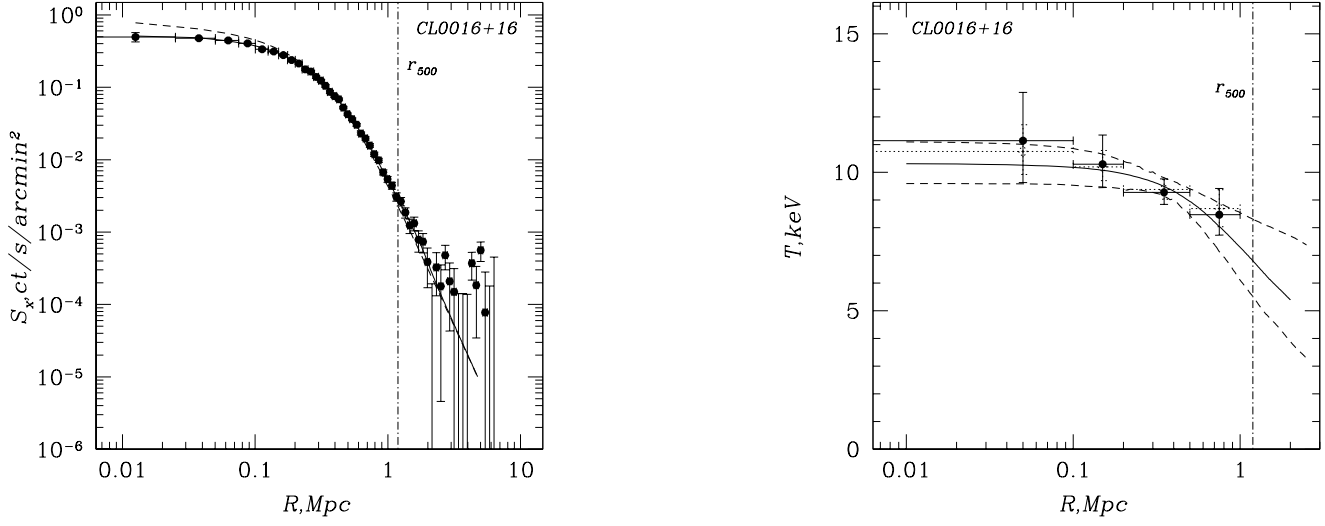


FIG. 4.— *Left:* Observed X-ray surface brightness profile (PN, MOS1,2 combined) of CL0016+16. Solid line shows the best fit  $\alpha$ - $\beta$  model convolved with the PSF. For comparison, dashed line shows the same model without the PSF degradation. *Right:* Solid circles show the deconvolved projected temperature profile. For comparison, open circles show the raw measurements from the X-ray fit in the same annuli. Solid line shows the best-fit projected temperature profile and dashed lines correspond to its 68% CL uncertainties.

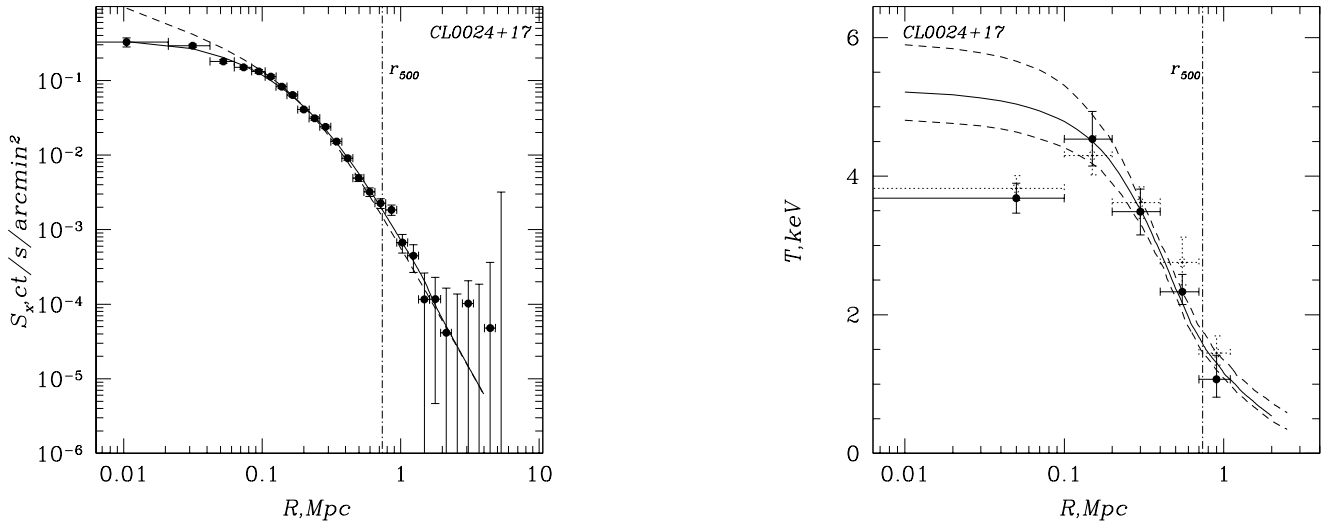


FIG. 5.— Same as Fig. 4, but for CL0024+17.

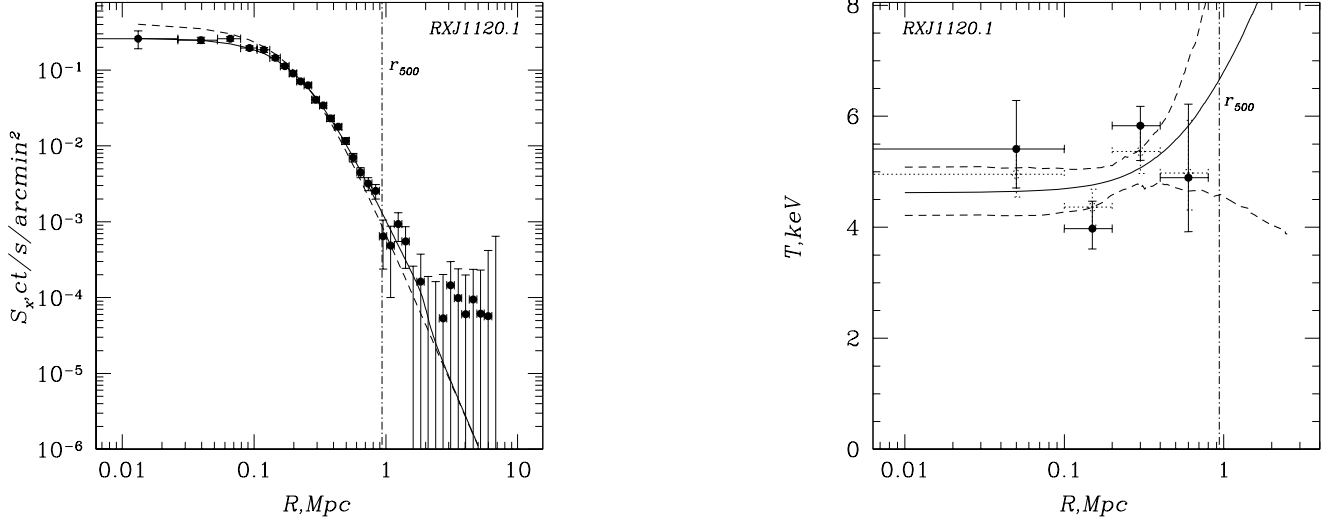


FIG. 6.— Same as Fig. 4, but for RXJ1120.1+4318

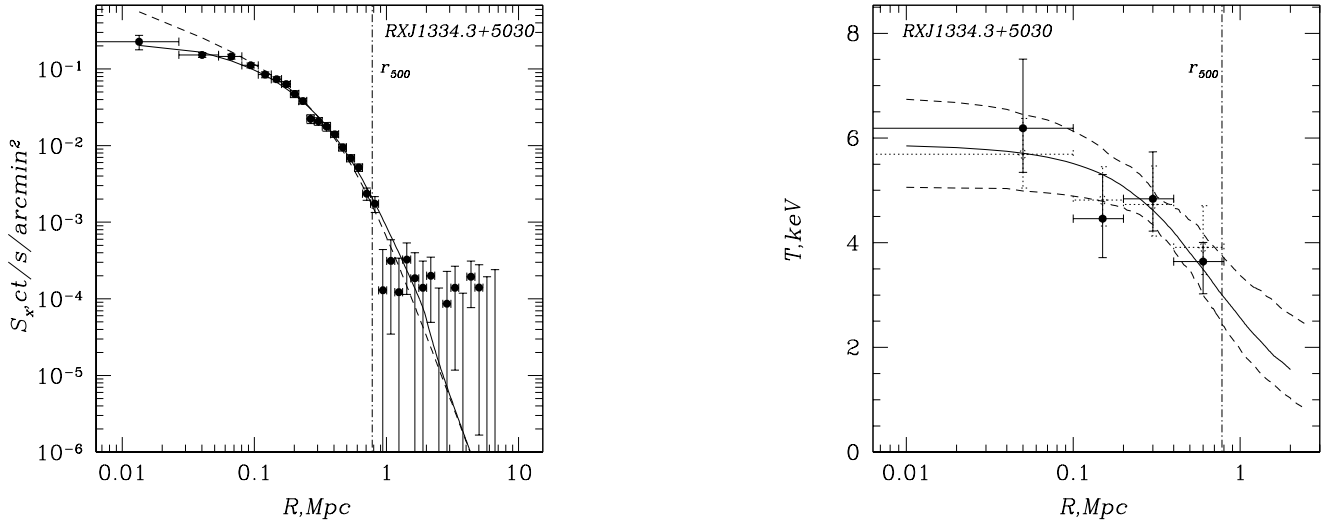


FIG. 7.— Same as Fig. 4, but for RXJ1334.3+5030.

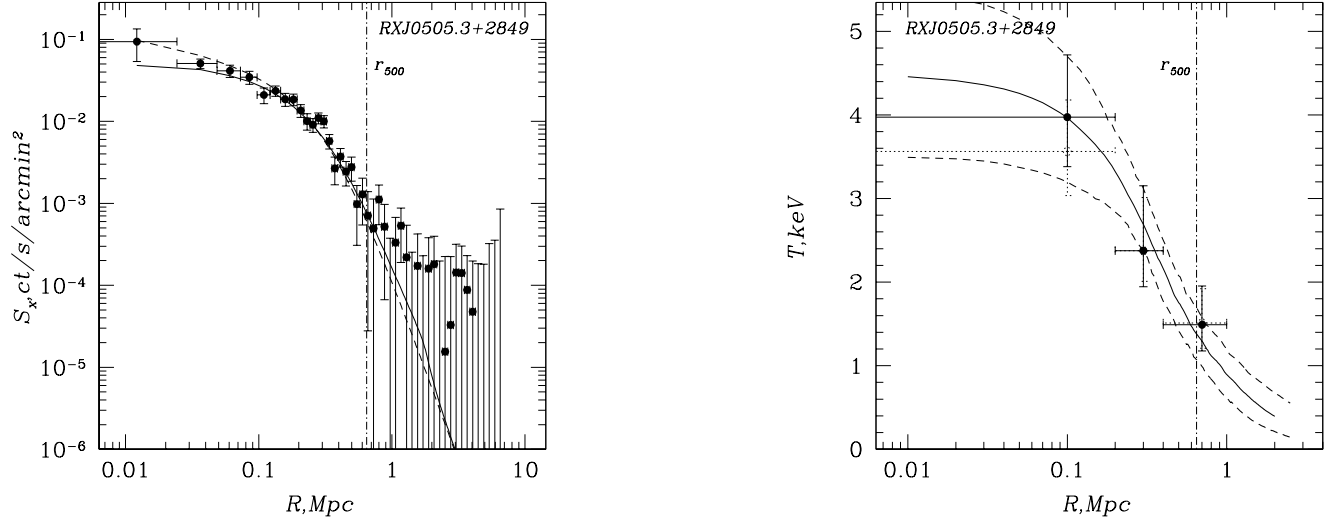


FIG. 8.— Same as Fig. 4, but for RXJ0505.3+2849.

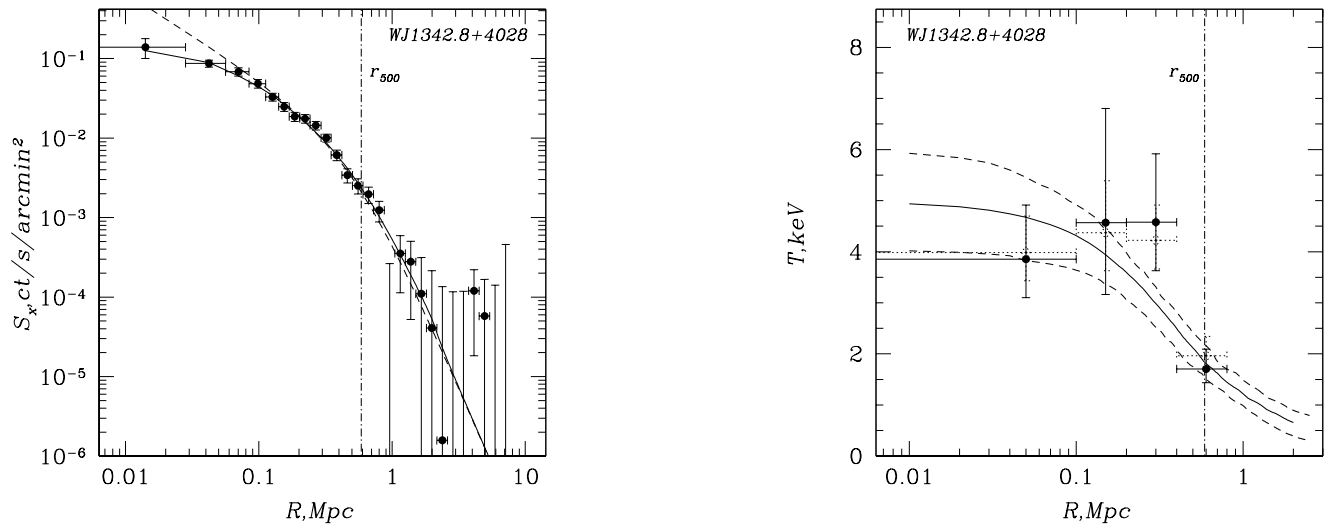


FIG. 9.— Same as Fig. 4, but for WJ1342.8+4028.

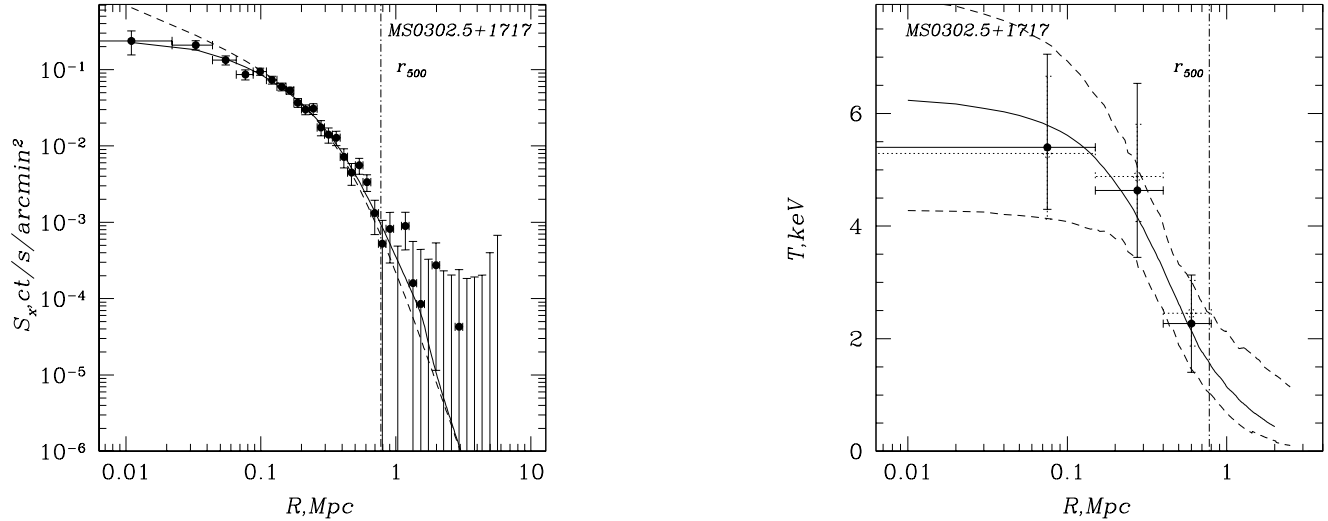


FIG. 10.— Same as Fig. 4, but for MS0302.5+1717.